

**Subpetahertz helicity-modulated high-order harmonic radiation**Xiaofan Zhang,<sup>1</sup> Liang Li,<sup>1</sup> Xiaosong Zhu,<sup>1,\*</sup> Kunlong Liu,<sup>2</sup> Xi Liu,<sup>1</sup> Dian Wang,<sup>1</sup> Pengfei Lan,<sup>1,†</sup>  
Ingo Barth,<sup>2,‡</sup> and Peixiang Lu<sup>1,3,§</sup><sup>1</sup>*Wuhan National Laboratory for Optoelectronics and School of Physics, Huazhong University of Science and Technology, Wuhan 430074, China*<sup>2</sup>*Max Planck Institute of Microstructure Physics, Weinberg 2, D-06120 Halle (Saale), Germany*<sup>3</sup>*Laboratory of Optical Information Technology, Wuhan Institute of Technology, Wuhan 430205, China*

(Received 1 December 2017; published 20 August 2018)

We demonstrate a scheme to produce coherent extreme ultraviolet and soft x-ray radiation with subpetahertz temporal helicity modulation, based on the high harmonic generation from current-carrying orbitals driven by intense linearly polarized laser fields. It is found that the electronic angular momentum of the orbitals oscillates periodically in femtosecond scale in the driving field. This so-far undescribed phenomenon is qualitatively interpreted and attributed to the laser-induced energy shift of orbitals. Consequently, the polarization of the harmonic radiation switches periodically in the temporal domain between left and right elliptical polarizations, and the frequency of the helicity modulation reaches subpetahertz. By varying the intensity of the laser field, the modulation frequency can be continuously controlled. This light source will serve as a potential tool to detect and manipulate the ultrafast dynamics in magnetic materials and chiral media.

DOI: [10.1103/PhysRevA.98.023418](https://doi.org/10.1103/PhysRevA.98.023418)**I. INTRODUCTION**

Ultrafast coherent radiation in extreme ultraviolet (XUV) and soft x-ray regions, with its novel and unique capabilities, provides an unprecedented tool to explore the features and dynamical processes of matter. The corresponding studies have shed light on numerous scientific areas such as atomic, molecular and optical physics, condensed matter physics, chemistry, biology, medicine, etc. [1–6]. Motivated by the abundant applications, generation of XUV and soft x-ray radiations has been intensely studied with paramount interest. To date, such coherent radiation has been available at some large-scale x-ray facilities, such as synchrotrons or free-electron lasers (FELs) with linear, elliptical, or circular polarization [7–10]. The duration of the synchrotron and FEL pulses is generally limited to the femtosecond timescale. In parallel, an alternative and complementary way based on the high harmonic generation (HHG) has been developed in the past decades [11–19]. The HHG light source, resulting from the extreme nonlinear response of matter to intense laser field, can be realized on a table-top scale, as opposed to the large synchrotrons and FEL facilities. Moreover, the pulse duration from the HHG is in the attosecond (as) timescale with the shortest record being 43 as [18]. As the natural time of electrons in atoms and molecules is in the subfemtosecond or attosecond regime, the radiation of HHG provides the capability to explore the real-time electronic dynamics with both high spatial and temporal resolutions [20–25].

The HHG process can be well understood with the three-step recollision model [26]. According to the recollision mechanism of HHG, it was believed to be impossible to efficiently generate nonlinearly polarized high harmonics for many years. Therefore, in the past decades, a vast majority of works only focused on the generation of the linearly polarized XUV and x-ray attosecond pulses. However, numerous works have shown that the circularly polarized (CP) and elliptically polarized (EP) XUV and x-ray radiations play significant roles in studying the chiral and magnetic properties and dynamics of matter [27–33]. Motivated by these important applications, experimental and theoretical efforts have been recently devoted to producing CP or EP high harmonics. To achieve the objective, one can both control the HHG process microscopically [31–41] and macroscopically [42]. The obtained CP or EP high harmonic radiations have been applied in different studies [43,44], for example, to extract the magneto-optical (MO) absorption coefficient of Co, Fe, and Gd from the x-ray magnetic circular dichroism (XMCD) measurements [32,33]. So far, the generated CP and EP XUV and soft x-ray radiations, from all the existing methods, are polarized with similar ellipticity and the same helicity (the sign of ellipticity indicating the rotation direction) in temporal domain. The ultrafast dynamical manipulation of the polarization has rarely been studied.

In our study, we demonstrate a scheme to produce coherent XUV and soft x-ray radiation with subpetahertz (sub-PHz) helicity modulation in temporal domain. The strategy is based on the HHG from a current-carrying orbital (CCO) [45–48] driven by a linearly polarized laser field, and is numerically demonstrated by solving the time-dependent Schrödinger equation (TDSE). We first show that, in the driving field, the time-dependent (TD) wave function evolves periodically between orbitals with opposite angular momenta. This intriguing phenomenon is qualitatively interpreted under adiabatic

\*zhuxiaosong@hust.edu.cn

†pengfeilan@hust.edu.cn

‡barth@mpi-halle.mpg.de

§lupeixiang@mail.hust.edu.cn

approximation and attributed to the different energy shifts of the instantaneous eigenstates. Then we show that, from this time-varying orbital, the helicity of the high harmonic radiation switches periodically over time between  $+1$  and  $-1$ . The frequency of the helicity modulation reaches sub-PHz and can be continuously adjusted by the intensity of the driving field.

The paper is arranged as follows: In Sec. II we briefly present the theoretical model. In Sec. III A, an intriguing phenomenon, i.e., an evolution of the TD wave function with ultrafast orbital angular momentum oscillation, is presented and interpreted based on the adiabatic approximation. In Sec. III B we demonstrate a scheme to produce coherent extreme ultraviolet and soft x-ray radiation with subpetahertz temporal helicity modulation based on this phenomenon. Finally, we summarize our findings in Sec. IV.

## II. THEORETICAL MODEL

In our simulation we numerically solve the 2D single-active-electron (SAE) time-dependent Schrödinger equation [49] [atomic units (a.u.) are used throughout this work unless otherwise stated]:

$$i \frac{\partial}{\partial t} |\Psi(t)\rangle = H(t) |\Psi(t)\rangle. \quad (1)$$

The Hamiltonian reads

$$H(t) = -\frac{1}{2} \nabla^2 + V(\vec{r}, t) + \vec{r} \cdot \vec{E}(t), \quad (2)$$

where  $\vec{E}(t)$  is the driving field. And the target atom is modeled by a 2D effective potential  $V(\vec{r}) = -Z(\vec{r})/\sqrt{\vec{r}^2 + \alpha}$ , where  $Z(\vec{r}) = 1 + 9 \exp(-\vec{r}^2)$  and  $\alpha = 2.88172$  to obtain the ionization potential of Ne  $I_p = 0.793$  a.u. for the  $2p$  orbitals [41,45]. The stationary normalized orbitals of the two degenerate states  $2p_x, y$ , denoted by  $|\phi_{2p_x}\rangle$  and  $|\phi_{2p_y}\rangle$ , are obtained by solving TDSE with imaginary time propagation. The CCO  $2p_{\pm}$  states for magnetic quantum numbers  $m = \pm 1$ , denoted by  $|\phi_{2p_{\pm}}\rangle$ , are calculated as  $|\phi_{2p_{\pm}}\rangle = (|\phi_{2p_x}\rangle \pm i|\phi_{2p_y}\rangle)/\sqrt{2}$  [41]. In the real-time propagation, the TD wave function  $\Psi(\vec{r}, t)$  is obtained by solving the TDSE using the split-operator technique [50], and the TD dipole acceleration can be calculated according to Ehrenfest theorem  $\vec{a}(t) = -\langle \Psi(\vec{r}, t) | \vec{\nabla} V(\vec{r}) - \vec{E}(t) | \Psi(\vec{r}, t) \rangle$ . Correspondingly, the  $x, y$  components of the harmonic radiation in the frequency domain are  $\vec{E}_{x,y}^h(\Omega) = \int a_{x,y}(t) e^{-i\Omega t} dt$ , in which  $\Omega$  is the photon energy of the harmonics. The radiation can also be divided into the left and right rotating components ( $\vec{E}_-^h$  and  $\vec{E}_+^h$ ), which are obtained as  $\vec{E}_{\pm}^h = (\vec{E}_x^h \pm i\vec{E}_y^h)/\sqrt{2}$ . In the following discussions we take the initial state of CCO  $2p_+$  as an example. The CCO can be obtained with CP pulses propagating along the  $z$  axis [46,51,52].

## III. RESULTS AND DISCUSSIONS

### A. Ultrafast oscillation of orbital angular momentum in a linearly polarized laser field

The schematic of the strategy is illustrated in Fig. 1, where the  $2p_+$  orbital is driven by an intense laser field propagating along the  $z$  axis. And the linear polarization direction of the driving field is defined as the  $x$  direction. The wavelength of the

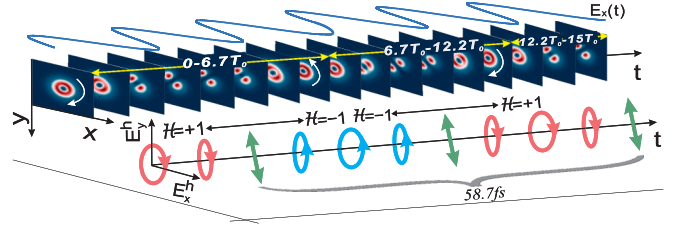


FIG. 1. Schematic of the strategy. The initial orbital is  $2p_+$  as an example. Contour plots show the snapshots of the EPD from 0 to  $15T_0$ . The electron rotating direction of the orbital is indicated by the white arrows.  $\mathcal{H}$  denotes the helicity of radiation. Red and blue circles indicate the radiations with  $\mathcal{H} = +1$  and  $\mathcal{H} = -1$ , respectively. The green arrows indicate the linearly polarized radiation with  $\mathcal{H} = 0$ . The wavelength of the driving laser is 1600 nm and the intensity is  $2 \times 10^{14}$  W/cm $^2$ .

driving laser is 1600 nm and the intensity is  $2 \times 10^{14}$  W/cm $^2$ . The pulse duration is  $24T_0$  with a trapezoidal envelope ( $2T_0$  rising and falling edges and  $20T_0$  plateau), in which  $T_0$  is the optical cycle of the driving field. The contour plots show snapshots of the electron probability density (EPD) of the wave functions at different times from  $t = 0$  to  $t = 15T_0$  during the TDSE propagation. The white arrows in the snapshots represent the electron rotating directions, which are determined from the phase of the wave function. Since the initial state is  $2p_+$ , the EPD at  $t = 0$  exhibits a toroidal distribution and the electron rotates anticlockwise [39,45]. With the evolution in the intense driving field, an intriguing phenomenon arises. The EPD varies prominently and periodically. In one period, the orbital gradually evolves from  $2p_+$  approximately to the dumbbell shaped orbital aligned at  $45^\circ$  (denoted as  $2p_{+45}$ ), then to the  $2p_-$  state, and finally to the  $2p_{-45}$ . The first period is about  $12.2T_0 = 65.1$  fs, which is a little longer than the following periods (about  $11T_0 = 58.7$  fs). This is because the electric field is weaker at the rising edge of the pulse, as will be discussed later.

The evolution of the TD wave function originates from the laser-dressed dynamics of orbitals and can be qualitatively interpreted by the following formulas under the adiabatic approximation. The TD wave function can be written as a superposition of instantaneous eigenstates of  $H(t)$  as

$$|\Psi(t)\rangle = \sum_{\lambda} c_{\lambda}(t) |\varphi_{\lambda}(t)\rangle e^{i\theta_{\lambda}(t)}, \quad (3)$$

where  $c_{\lambda}(t)$  are TD coefficients,  $\theta_{\lambda}(t) = -\int_0^t \varepsilon'_{\lambda}(\tau) d\tau$ .  $|\varphi_{\lambda}(t)\rangle$  are the instantaneous eigenstates satisfying  $H(t) |\varphi_{\lambda}(t)\rangle = \varepsilon'_{\lambda}(t) |\varphi_{\lambda}(t)\rangle$ .  $\varepsilon'_{\lambda}(t)$  is the TD instantaneous eigenenergy. Substituting Eq. (3) into Eq. (1), one gets  $\dot{c}_{\lambda}(t) = e^{i\gamma_{\lambda}(t)} c_{\lambda}(0)$ , i.e.,  $|\Psi(t)\rangle = \sum_{\lambda} c_{\lambda}(0) |\varphi_{\lambda}(t)\rangle e^{i\theta_{\lambda}(t) + i\gamma_{\lambda}(t)}$ , where  $\gamma_{\lambda}(t) = i \int_0^t \langle \varphi_{\lambda}(\tau) | \dot{\varphi}_{\lambda}(\tau) \rangle d\tau$  is real [53]. According to the initial condition  $|\Psi(t=0)\rangle = (|\phi_{2p_x}\rangle + i|\phi_{2p_y}\rangle)/\sqrt{2}$ , one can get

$$\begin{aligned} |\Psi(t)\rangle &= c_1(0) e^{i\theta_1(t) + i\gamma_1(t)} |\varphi_1(t)\rangle + c_2(0) e^{i\theta_2(t) + i\gamma_2(t)} |\varphi_2(t)\rangle \\ &= \frac{1}{\sqrt{2}} e^{i\theta_1(t) + i\gamma_1(t)} |\varphi_1(t)\rangle + \frac{i}{\sqrt{2}} e^{i\theta_2(t) + i\gamma_2(t)} |\varphi_2(t)\rangle, \end{aligned} \quad (4)$$

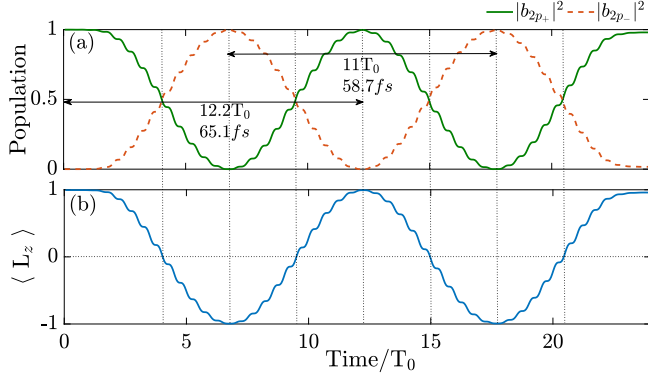


FIG. 2. (a) The populations on the  $2p_+$  (solid green curve) and  $2p_-$  (dashed red curve) states as a function of time. The first modulation period is  $12.2T_0 = 65.1$  fs and the following ones are  $11T_0 = 58.7$  fs. (b) The expectation value of angular momentum ( $L_z$ ) as a function of time. The laser parameters are the same as those in Fig. 1.

where  $|\varphi_1(t=0)\rangle = |\phi_{2p_x}\rangle$  and  $|\varphi_2(t=0)\rangle = |\phi_{2p_y}\rangle$ . In the laser field,  $|\varphi_{1,2}(t)\rangle$  are always very close to  $|\phi_{2p_{x,y}}\rangle$  (the features of  $|\varphi_1\rangle$  and  $|\varphi_2\rangle$  are discussed in detail in Appendix A). Note that, although a simple form with only two terms is obtained in Eq. (4), no approximation is used to neglect the excited eigenstates. Namely, in the field-free eigenstate basis, all the states, including the  $2p_+$ ,  $2p_-$  and other excited states,

are taken into account in the evolution of  $|\Psi(t)\rangle$  in Eq. (4). Equation (4) provides a simple interpretation for the evolution of the time-dependent wave function: the dynamical evolution can be understood by the coherent superposition of  $|\varphi_1(t)\rangle$  and  $|\varphi_2(t)\rangle$  with different time-dependent phases. As the relative phase changes with time, the superposed wave function  $|\Psi(t)\rangle$  varies periodically as indicated in Fig. 1.

To have a deeper insight into the phenomenon and the oscillation period of the EPD, we also project the TD wave function  $\Psi(\vec{r}, t)$  shown in Fig. 1 onto the field-free eigenstates  $|\phi_\mu\rangle$  and obtain the populations on the eigenstates  $|\phi_\mu\rangle$  as  $|b_\mu(t)e^{-i\varepsilon_\mu t}|^2 = |\langle\phi_\mu|\Psi(t)\rangle|^2$ , which satisfies  $\sum_\mu |b_\mu(t)|^2 = 1$ .  $\varepsilon_\mu$  is the eigenenergy of the field-free state  $|\phi_\mu\rangle$ . The populations on the  $2p_\pm$  states  $|b_{2p_\pm}(t)|^2$  are shown in Fig. 2(a). One can see that  $|b_{2p_\pm}(t)|^2$  are periodically oscillated, resembling cosine-like functions with opposite phases. The oscillation period is the same as that in Fig. 1. Herein, since  $\sum_{\mu \neq 2p_\pm} |b_\mu|^2 \ll |b_{2p_+}|^2 + |b_{2p_-}|^2 \approx 1$ , i.e., the populations on the other states are negligible compared to those on  $2p_+$  and  $2p_-$  states, we will focus on  $|b_{2p_\pm}(t)|^2$  when discussing the EPD and angular momentum of the TD wave function.

According to Eq. (4), one can obtain the analytical expression of the populations  $|b_{2p_\pm}(t)|^2$ . Since the applied linear laser field is too weak to essentially distort the wave functions  $\varphi_1(t)$  and  $\varphi_2(t)$  (see Appendix A), one can approximate  $\langle\varphi_1(t)|\phi_{2p_y}\rangle \approx 0$  and  $\langle\varphi_2(t)|\phi_{2p_x}\rangle \approx 0$ . Then, by calculating the inner product  $\langle\phi_{2p_\pm}|\Psi(t)\rangle$  in Eq. (4), one can obtain the populations of  $2p_\pm$  orbitals as

$$\begin{aligned} |b_{2p_\pm}(t)|^2 &= \left| \frac{1}{\sqrt{2}} \langle\phi_{2p_x} \pm i\phi_{2p_y} | \frac{1}{\sqrt{2}} e^{i\theta_1(t)+i\gamma_1(t)} \varphi_1(t) + \frac{i}{\sqrt{2}} e^{i\theta_2(t)+i\gamma_2(t)} \varphi_2(t) \right\rangle e^{i\varepsilon_{2p_\pm} t} \right|^2 \\ &= \frac{1}{2} |b_{2p_x}(t)|^2 + \frac{1}{2} |b_{2p_y}(t)|^2 \pm |b_{2p_x}(t)||b_{2p_y}(t)| \cos[\xi(t)t + \kappa(t)], \end{aligned} \quad (5)$$

where  $|b_{2p_x}(t)| = \frac{1}{\sqrt{2}} |\langle\phi_{2p_x}|\varphi_1(t)\rangle|$ ,  $|b_{2p_y}(t)| = \frac{1}{\sqrt{2}} |\langle\phi_{2p_y}|\varphi_2(t)\rangle|$ ,  $\xi(t) = \frac{1}{t} \int_0^t [\Delta\varepsilon'_2(\tau) - \Delta\varepsilon'_1(\tau)] d\tau$ ,  $\kappa(t) = \gamma_2(t) - \gamma_1(t)$ ,  $\Delta\varepsilon'_{1,2}(t) = \varepsilon'_{1,2}(t) - \varepsilon'_{1,2}(0) = \varepsilon'_{1,2}(t) - \varepsilon_{2p_{x,y}}$ , and  $\varepsilon_{2p_{x,y}}$  are the eigenenergies of  $2p_{x,y}$  orbitals. Note that we neglected the small quantities with  $|b_{\mu \neq 2p_\pm}|$  when deriving Eq. (5). This approximation is used only when we are discussing observables like the EPD and the angular momentum. However, this does not mean the evolution of  $|\Psi(t)\rangle$  involves only the field-free  $2p_\pm$  states. All the excited states are also included in the instantaneous eigenstates and in  $|\Psi(t)\rangle$ . Considering  $\frac{1}{2}(|b_{2p_x}|^2 + |b_{2p_y}|^2) = \frac{1}{2}(|b_{2p_+}|^2 + |b_{2p_-}|^2) \approx 1$ , the summation of the first two terms in Eq. (5) is almost constant. The last term in Eq. (5) exhibits a cosine-like oscillation. The frequency of the oscillation is determined by the average of  $\xi(t)$ , and the fluctuation of  $\xi(t)$  leads to the tiny modulation in the  $|b_{2p_\pm}(t)|^2$  curves. One can see that the oscillation of  $|b_{2p_\pm}(t)|^2$  in Fig. 2 is well interpreted by Eq. (5). The oscillation can be also understood by the STIRAP-like process via field-free excited states [54].

Furthermore, based on the relationships  $\phi_{2p_\pm} = \frac{\phi_{2p_x} \pm i\phi_{2p_y}}{\sqrt{2}}$  and  $\phi_{2p_\pm} = |\phi_{2p}| e^{\pm i\eta}$ , one can get  $\frac{\phi_{2p_x}}{\sqrt{2}} = |\phi_{2p}| \cos(\eta)$  and  $\frac{\phi_{2p_y}}{\sqrt{2}} = |\phi_{2p}| \sin(\eta)$ , where  $\eta$  is the angle. Considering that the EPD can be expanded with the field-free eigenstates as  $|\Psi(\vec{r}, t)|^2 = |\sum_\mu b_\mu(t)\phi_\mu(\vec{r})|^2$  and neglecting the small terms with  $|b_{\mu \neq 2p_\pm}|$  in the expansion, one can get

$$\begin{aligned} |\Psi(\vec{r}, t)|^2 &= |b_{2p_+}(t)|^2 |\phi_{2p}|^2 + |b_{2p_-}(t)|^2 |\phi_{2p}|^2 + 2|b_{2p_+}(t)||b_{2p_-}(t)||\phi_{2p}|^2 \{\cos[2\eta + \Delta\Phi(t)]\} \\ &= [ |b_{2p_+}(t)| - |b_{2p_-}(t)| ]^2 |\phi_{2p}|^2 + 4|b_{2p_+}(t)||b_{2p_-}(t)||\phi_{2p}| \cos\left(\eta + \frac{\Delta\Phi(t)}{2}\right)^2 \\ &= [ |b_{2p_+}(t)| - |b_{2p_-}(t)| ]^2 |\phi_{2p}|^2 + 2|b_{2p_+}(t)||b_{2p_-}(t)| \left[ \phi_{2p_x} \cos\left(\frac{\Delta\Phi(t)}{2}\right) - \phi_{2p_y} \sin\left(\frac{\Delta\Phi(t)}{2}\right) \right]^2, \end{aligned} \quad (6)$$

where  $\Delta\Phi(t) = \arg[b_{2p_+}(t)/b_{2p_-}(t)]$ . In Eq. (6), the first term exhibits isotropic distribution. The second term exhibits a

dumbbell shaped distribution, which is aligned at the angle of  $-\Delta\Phi(t)/2$  relative to the  $x$  axis. Both the TDSE simulation

and our model indicate that  $\Delta\Phi(t)$  is (approximately) either  $-\pi/2$  or  $\pi/2$  (see Appendix B). Therefore, the EPD exhibits the  $2p_{\pm 45}$ -like distributions when  $|b_{2p_+}| = |b_{2p_-}|$ , and exhibits the isotropic  $2p_{\pm}$ -like distribution when  $|b_{2p_+}(t)|^2$  or  $|b_{2p_-}(t)|^2$  reaches 0.

With the periodical evolution of the TD wave function, the  $z$  component of the orbital angular momentum  $L_z$  oscillates periodically. In Fig. 2(b) we calculate the expectation value of  $L_z$  by  $\langle \hat{L}_z \rangle = \langle \Psi(t) | \frac{1}{i} (x \frac{\partial}{\partial y} - y \frac{\partial}{\partial x}) | \Psi(t) \rangle$ . One can see that  $\langle \hat{L}_z \rangle$  oscillates between +1 and -1 resembling a cosine-like function, which varies in phase with  $|b_{2p_+}(t)|^2$  and in antiphase with  $|b_{2p_-}(t)|^2$  in Fig. 2(a). This correspondence between  $|b_{2p_{\pm}}(t)|^2$  and  $\langle \hat{L}_z \rangle$  can be intuitively understood:  $\langle \hat{L}_z \rangle = \langle \sum_{\mu} b_{\mu}(t) \phi_{\mu} | \frac{1}{i} (x \frac{\partial}{\partial y} - y \frac{\partial}{\partial x}) | \sum_{\mu} b_{\mu}(t) \phi_{\mu} \rangle = \sum_{\mu} |b_{\mu}(t)|^2 L_{z,\mu}$ , where  $L_{z,\mu} = \langle \phi_{\mu} | \frac{1}{i} (x \frac{\partial}{\partial y} - y \frac{\partial}{\partial x}) | \phi_{\mu} \rangle$ . Considering the  $z$  components of angular momentum of the  $2p_{\pm}$  states are  $L_{z,2p_{\pm}} = \pm 1$  and  $\langle \hat{L}_z \rangle \approx |b_{2p_+}|^2 L_{z,2p_+} + |b_{2p_-}|^2 L_{z,2p_-}$  after neglecting the small terms with  $|b_{\mu \neq 2p_{\pm}}|^2$ , one can get  $\langle \hat{L}_z \rangle = |b_{2p_+}|^2 - |b_{2p_-}|^2$ . Note that, although all the above discussions are based on the condition that  $\sum_{\mu \neq 2p_{\pm}} |b_{\mu}|^2 \ll |b_{2p_+}|^2 + |b_{2p_-}|^2$ , similar phenomenon of the evolution exists when stronger laser field is applied and the evolution can also be approximately interpreted with the same method.

Our proposed scheme is based on the phenomenon accompanied by the fast oscillation of the angular momentum. Recent works have shown that the angular momentum  $L_z$  of the electronic state can be imprinted on the polarization of the high harmonic radiation [39,41,55]. Specifically, orbitals with positive  $L_z$  ( $m > 0$ ) will predominately generate high harmonics with positive helicity and those with negative  $L_z$  ( $m < 0$ ) are more likely to generate high harmonics with negative helicity [41,55]. In our case, if the TD orbital is dominantly contributed by  $2p_+$ , the radiation is predominately EP with positive helicity. If the TD orbital is dominantly contributed by  $2p_-$ , the radiation is more likely to be EP with negative helicity. Therefore, as illustrated by the arrows and circles in the last line of Fig. 1, the generated emissions from the initial CCO  $2p_+$  driven by the linearly polarized laser field will be modulated correspondingly between left and right elliptical polarization.

### B. High harmonic radiation from the time-varying orbitals with angular momentum oscillation

Figure 3 shows the high harmonic spectra in frequency domain generated by the TD wave function in Fig. 1. The solid blue curve displays the harmonic spectrum for the left rotating component and the dashed red curve represents the harmonic spectrum for the right rotating component. For clarity, the harmonic spectra in the range of [100, 110] orders are plotted in the inset. It is shown that the left and right rotating components are close to each other, i.e., the ellipticity of the total high harmonics in the harmonic spectrum is close to zero. This is because the high harmonic spectrum shows the time-integrated features of the harmonic emission in the frequency domain. Since we focus on the helicity oscillation in temporal domain in this work, time-resolved analysis characterizations for the harmonic emission are needed.

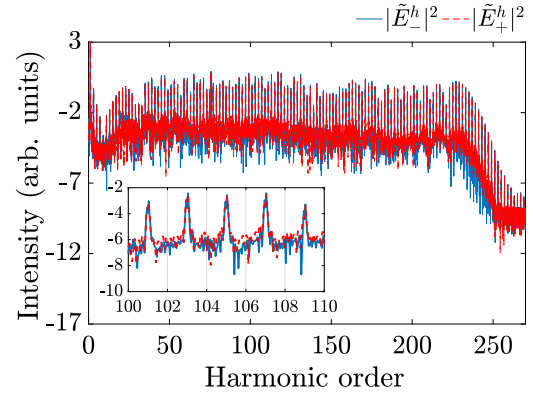


FIG. 3. The high harmonic spectra from the  $2p_+$  orbital. The laser parameters are the same as those in Fig. 1. The inset shows the harmonic spectra in the range of [100, 110] orders. The dashed red and solid blue curves represent the harmonic spectra for the right and left rotating components, respectively.

To demonstrate our strategy, we present the ellipticity distribution  $\epsilon(\Omega, t)$  of the obtained harmonic radiation in Fig. 4.  $\epsilon(\Omega, t)$  can be obtained by  $\epsilon(\Omega, t) = \frac{|GT_+(\Omega, t)| - |GT_-(\Omega, t)|}{|GT_+(\Omega, t)| + |GT_-(\Omega, t)|}$ , where  $GT_{\pm}(\Omega, t)$  are calculated by Gabor transform of  $\tilde{E}_{\pm}^h(\Omega)$  [56]. For clarity, the signals with intensity eight order of magnitude weaker than that in the plateau are filtered out in the distribution. As shown in Fig. 4, the ellipticity varies between positive and negative values periodically, i.e., the radiation varies between left and right elliptical polarization periodically. In Fig. 4(b) the laser parameters are the same as those in Fig. 1 and the period of the ellipticity modulation is also 58.7 fs in the plateau region of the driving laser. The high harmonics are generated via the common three-step mechanism [26]. However, in contrast to the HHG process studied in previous works, the state, where the continuum electrons tunnel from and recombine to, changes substantially over time in this work, which leads to the ultrafast temporal modulation of the emitted light. According to Eq. (5), the modulation period is dependent on  $\xi(t)$  and therefore can be continuously tuned by the laser intensity. With the increase of the intensity,  $\xi(t)$  increases and the modulation period decreases correspondingly. In Figs. 4(a) and 4(c) we present the harmonic ellipticity distributions with different laser intensities  $1 \times 10^{14}$  and  $3 \times 10^{14}$  W/cm<sup>2</sup>, respectively. The other laser parameters are the same as those

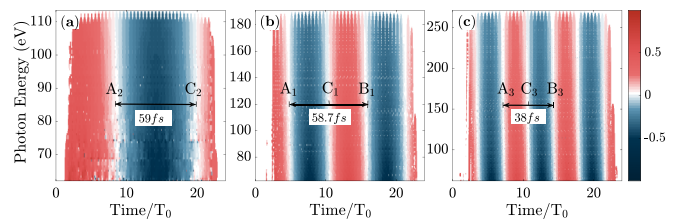


FIG. 4. Ellipticity distribution of the harmonic radiation versus photon energy and time for three different laser intensities: (a)  $1 \times 10^{14}$  W/cm<sup>2</sup>, (b)  $2 \times 10^{14}$  W/cm<sup>2</sup>, and (c)  $3 \times 10^{14}$  W/cm<sup>2</sup>. The other laser parameters are the same as those in Fig. 1. The double arrow lines indicate the half-period (a) and period (b) and (c) of the helicity modulation.

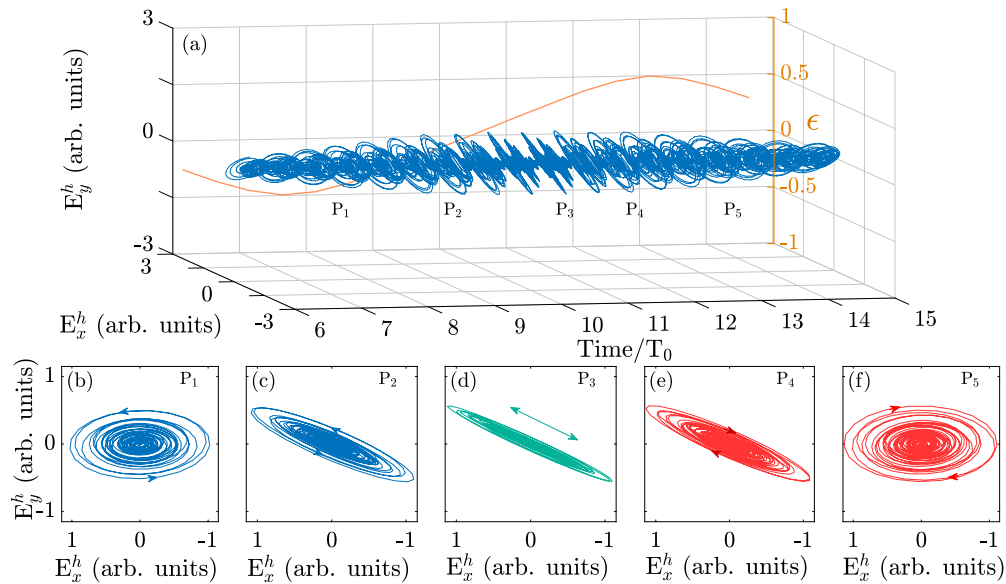


FIG. 5. Elliptically polarized electric field with helicity modulation obtained by synthesizing 62 to 85 eV high harmonics. (a) The temporal profile of the attosecond pulses is presented by the 3D blue curve. The orange curve on the time- $\epsilon$  plane shows the ellipticity of the radiation. (b)–(f) The projections of the pulses at  $P_1$  to  $P_5$  labeled in (a) on the  $E_x^h$ - $E_y^h$  plane. The laser parameters are the same as those in Fig. 1.

in Fig. 1. One can also see the helicity modulation, while the period is prominently changed. As shown in Fig. 4(a), the period is about  $22T_0$ , i.e., 118 fs. In Fig. 4(c) the period is about  $7.2T_0$ , i.e., 38 fs. With various intensities, the modulation period can be adjusted in a wide range in the femtosecond level. The relation between the modulation period and the intensity also explains the above-mentioned fact that the first period is longer than the ones in the plateau region of the driving laser. Regarding the photon energy of the harmonics, one can see that the maxima of the photon energy reach 120, 200, and 270 eV in Figs. 4(a)–4(c), respectively, indicating that the bursts can cover the XUV and soft x-ray regions. Figure 4 shows that, with our scheme, the generation of helicity-modulated coherent XUV and soft x-ray radiations with continuously tunable sub-PHz modulation frequency can be achieved. Our result is different from the intuitive consideration that the emission should have the same helicity as that of the initial orbital, because in this work the dynamics of the laser-dressed orbitals play a significant role [16,57–59].

Finally, we present results of the emission in the temporal domain between  $6T_0$  and  $15T_0$  (covering one half modulation period) in Fig. 5(a). The electric field of the radiation in the temporal domain is obtained by synthesizing the high harmonics in the spectrum range of  $[\Omega_1, \Omega_2]$  as  $E_{x,y,\pm}^h(t) = \int_{\Omega_1}^{\Omega_2} \tilde{E}_{x,y,\pm}^h(\Omega) e^{i\Omega t} d\Omega$ . Here the range is [62 eV, 85 eV]. The laser parameters are the same as those in Fig. 1. The corresponding ellipticity in temporal domain is  $\epsilon(t) = \frac{|E_x^h(t)| - |E_y^h(t)|}{|E_x^h(t)| + |E_y^h(t)|}$ , which is also presented in the time- $\epsilon$  plane. For clarity, projections of the five pulses on the  $E_x^h$ - $E_y^h$  plane near  $7.5T_0$ ,  $9T_0$ ,  $10.5T_0$ ,  $11.5T_0$ , and  $13T_0$  labeled by  $P_1$  to  $P_5$  are plotted in Figs. 5(b)–5(f), respectively. From Fig. 5 one can clearly see the evolution of the radiation, from left elliptical polarization to linear polarization and right elliptical polarization. We also present the results from the  $1s$  orbital in Appendix C and

make a comparison with the results from the  $2p_+$  orbital to demonstrate how large the predicted effect is. The comparison further indicates that the angular momentum of the target orbital plays a significant role in the polarization state of the harmonic emission. Such an ultrafast helicity-modulated light source can be experimentally observed by a so-far developed 3D attosecond metrology [60]. This temporal profile is like a polarization gating in the XUV and femtosecond regions. The ellipticity reaches up to 0.5. In the result, the contributions of both short and long trajectories are found. In experiments, one can filter out the short or long trajectory with the propagation effect [61], and attosecond pulse train with sub-PHz helicity modulation can be obtained. In Fig. 5 the duration of the pulses is about 160 as. To further confirm the physical effect, we have also carried out the 3D calculations. One can see that the same phenomenon and results are obtained (see Appendix D).

#### IV. CONCLUSION

In conclusion, we discovered and studied a so-far undescribed dynamical process that, when the CCO is exposed to a linearly polarized laser field, the state evolves periodically between CCO with opposite angular momenta. Based on HHG from this time-varying wave function, we demonstrated a strategy to generate coherent XUV and soft x-ray radiations with ultrafast helicity modulation in temporal domain. The frequency of the modulation is continuously tunable in a wide range in the sub-PHz level. This light source provides an elegant and efficient route for probing and manipulating the ultrafast magnetic and chiral dynamics, like the onset of magnetization and demagnetization [62], ultrafast control of information in magnetic recording media [63], opto-magnetic switching [64], etc. We expect the light source can be used in other regions, such as the high-speed data processing and storage and petahertz electronics in solids.

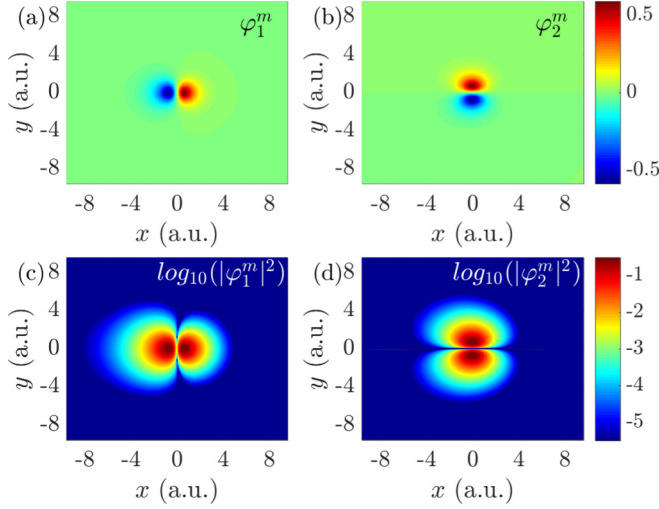


FIG. 6. The instantaneous wave functions (a)  $\varphi_1^m(\vec{r})$  and (b)  $\varphi_2^m(\vec{r})$ . The log plots of (c)  $\log_{10}[|\varphi_1^m(\vec{r})|^2]$  and (d)  $\log_{10}[|\varphi_2^m(\vec{r})|^2]$ .

### ACKNOWLEDGMENTS

The authors gratefully acknowledge helpful discussions with Professor Manfred Lein. This work was supported by National Natural Science Foundation of China (NSFC) under Grants No. 11774109, No. 11627809, and No. 11574101, and by the Max Planck Society for the Max Planck Research Group “Current-Carrying Quantum Dynamics” (CCQD) and the Deutsche Forschungsgemeinschaft, Priority Programme 1840 “Quantum Dynamics in Tailored Intense Fields” (QUTIF).

### APPENDIX A: EVALUATION OF THE INSTANTANEOUS EIGENSTATES AND $|b_{2p_{\pm}}|^2$ UNDER THE ADIABATIC APPROXIMATION

The instantaneous eigenstates  $|\varphi_{\lambda}(t)\rangle$  can be evaluated under the adiabatic approximation by diagonalizing the time-dependent Hamiltonian  $H(t) = H_0 - xE_x(t)$  with corresponding  $E_x(t)$ .

Figures 6(a) and 6(b) show the obtained instantaneous wave functions  $\varphi_1(\vec{r}, t)$  and  $\varphi_2(\vec{r}, t)$  when the electric field  $E_x(t)$  reaches its maximum 0.0755 a.u. [denoted as  $\varphi_1^m(\vec{r})$  and  $\varphi_2^m(\vec{r})$ ]. Figures 6(c) and 6(d) present the log plots of the squared modulus of  $\varphi_{1,2}^m(\vec{r})$ . It is shown that, although  $|\varphi_1^m\rangle$  and  $|\varphi_2^m\rangle$  are dressed by the laser field, they are still very close to the field-free states  $|\phi_{2p_x}\rangle$  and  $|\phi_{2p_y}\rangle$ , respectively. The nodal plane of  $|\varphi_2^m\rangle$  is still along the  $x$  axis, while the nodal plane of  $|\varphi_1^m\rangle$  is only slightly bent.

By numerically calculating the projections of the instantaneous eigenstates  $|\varphi_{1,2}^m\rangle$  onto the field-free states  $|\phi_{2p_{x,y}}\rangle$ , one can get

$$\begin{aligned} \langle \varphi_1^m | \phi_{2p_x} \rangle &= 0.993653, \\ \langle \varphi_2^m | \phi_{2p_x} \rangle &= 0.001183, \\ \langle \varphi_1^m | \phi_{2p_y} \rangle &= -0.001189, \\ \langle \varphi_2^m | \phi_{2p_y} \rangle &= 0.998799. \end{aligned} \quad (\text{A1})$$

These calculated projections further indicate that, as the laser field used in this work is too weak to substantially distort the

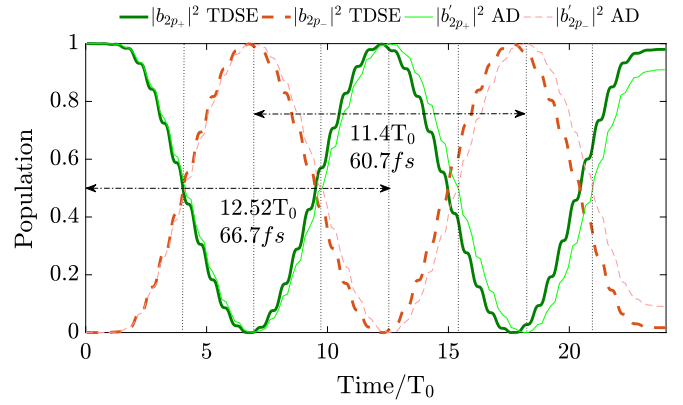


FIG. 7. The thin (light gray) curves show the populations  $|b_{2p_{\pm}}(t)|^2$  obtained based on Eq. (5) under the adiabatic approximation (labeled as “AD”). The results from the TDSE calculation (shown in Fig. 2) are also plotted by the thick (dark gray) curves (labeled as “TDSE”) for comparison.

wave functions  $\varphi_1(t)$  and  $\varphi_2(t)$ , the instantaneous eigenstates  $|\varphi_1(t)\rangle$  and  $|\varphi_2(t)\rangle$  are still very close to the field-free states  $|\phi_{2p_x}\rangle$  and  $|\phi_{2p_y}\rangle$ , respectively.

From the diagonalization of  $H(t) = H_0 - xE_x(t)$ , the instantaneous eigenenergy  $\varepsilon_{\lambda}'(t)$  and consequently  $\Delta\varepsilon_{1,2}'$  can also be evaluated. The dashed curves in Fig. 7 present the calculated  $|b_{2p_{\pm}}(t)|^2$  by substituting the results obtained from the diagonalization into Eq. (5). Meanwhile, the values of  $|b_{2p_{\pm}}(t)|^2$  obtained from the TDSE simulation [i.e., the two curves shown in Fig. 2(a)] are also plotted by the solid curves in Fig. 7.

Comparing the dashed curves to the solid curves, one can see that the cosine-like oscillation of populations on the field-free  $2p_{\pm}$  states is well reproduced. In the results from Eq. (5), the first period is  $12.5T_0$  and the following periods are  $11.4T_0$ , which are very close to the periods obtained from the TDSE simulation. The agreement between the results from the adiabatic approximation and those from the TDSE simulation indicates that our model well explains the evolution of the time-dependent wave function and the adiabatic approximation is valid in qualitatively analyzing this phenomenon. According to our numerical results under the adiabatic approximation,  $\kappa \approx 0$  in Eq. (5). Therefore, the frequency of the oscillation is determined by the average of  $\xi$ , and the fluctuation of  $\xi(t)$  also leads to the tiny modulation in the  $|b_{2p_{\pm}}(t)|^2$  curves.

From the results shown in Fig. 7, the periodic oscillation of the two populations  $|b_{2p_+}(t)|^2$  and  $|b_{2p_-}(t)|^2$  looks very much like Rabi oscillations. This is because the populations on the  $2p_+$  and  $2p_-$  states are dominating, i.e.,  $|b_{2p_+}(t)|^2 + |b_{2p_-}(t)|^2 \gg \sum_{\mu \neq 2p_{\pm}} |b_{\mu}(t)|^2$ . According to our discussions in this paper, the underlying mechanism actually differs from the Rabi oscillations between two field-free  $2p_{\pm}$  states.

### APPENDIX B: THE PHASE DIFFERENCE BETWEEN $b_{2p_+}(t)$ AND $b_{2p_-}(t)$

Based on our model, the time-dependent evolution of the EPD can be described with Eq. (6), where the phase difference  $\Delta\Phi(t)$  between  $b_{2p_+}(t)$  and  $b_{2p_-}(t)$  plays a significant role. In the TDSE simulation, it is shown that  $\Delta\Phi(t)$  is approximately

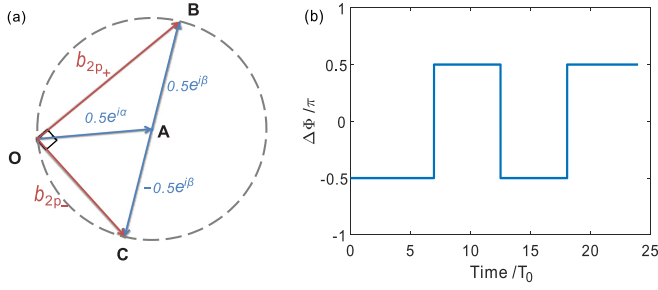


FIG. 8. (a) Analysis for Eq. (B4) based on the rotation vector method. (b) The relative phase between  $b_{2p_+}(t)$  and  $b_{2p_-}(t)$  obtained based on Eq. (B1) under the adiabatic approximation.

either  $-\pi/2$  or  $\pi/2$ . This can be intuitively understood based on the following equations with the help of the rotation vector method. By calculating the inner product  $\langle\phi_{\pm}|\Psi(t)\rangle$  in Eq. (4), one can obtain

$$b_{2p_{\pm}}(t) = \frac{1}{\sqrt{2}} \left\langle \phi_{2p_x} \pm i\phi_{2p_y} \left| \frac{1}{\sqrt{2}} e^{i\theta_1(t)+i\gamma_1(t)} \varphi_1(t) + \frac{i}{\sqrt{2}} e^{i\theta_2(t)+i\gamma_2(t)} \varphi_2(t) \right. \right\rangle e^{i\varepsilon_{2p_{\pm}} t}. \quad (\text{B1})$$

Since the applied laser field is too weak to essentially distort the wave functions  $\varphi_1(t)$  and  $\varphi_2(t)$  [as shown by the numerical calculations Eq. (A1)], one can approximate  $\langle\varphi_2(t)|\phi_{2p_x}\rangle \approx 0$ ,  $\langle\varphi_1(t)|\phi_{2p_y}\rangle \approx 0$ .

Then Eq. (B1) is simplified to

$$b_{2p_{\pm}}(t) = \frac{1}{2} \langle \phi_{2p_x} | \varphi_1(t) \rangle e^{-i \int_0^t \Delta\varepsilon'_1(\tau) d\tau + i\gamma_1(t)} \pm \frac{1}{2} \langle \phi_{2p_y} | \varphi_2(t) \rangle e^{-i \int_0^t \Delta\varepsilon'_2(\tau) d\tau + i\gamma_2(t)}, \quad (\text{B2})$$

with  $\Delta\varepsilon'_{1,2}(t) = \varepsilon'_{1,2}(t) - \varepsilon'_{1,2}(0) = \varepsilon'_{1,2}(t) - \varepsilon_{2p_{x,y}}$ .

For simplicity we define

$$\alpha \equiv - \int_0^t \Delta\varepsilon'_1(\tau) d\tau + \gamma_1(t),$$

$$\beta \equiv - \int_0^t \Delta\varepsilon'_2(\tau) d\tau + \gamma_2(t), \quad (\text{B3})$$

and assume that  $\langle\varphi_{2p_x}|\phi_1(t)\rangle = 1$  and  $\langle\varphi_{2p_y}|\phi_2(t)\rangle = 1$ . In this case, Eq. (B2) is simplified to

$$b_{2p_+}(t) = \frac{1}{2} e^{i\alpha} + \frac{1}{2} e^{i\beta},$$

$$b_{2p_-}(t) = \frac{1}{2} e^{i\alpha} - \frac{1}{2} e^{i\beta}. \quad (\text{B4})$$

In Fig. 8(a) the vectors  $\vec{OA}$ ,  $\vec{AB}$ , and  $\vec{AC}$  represent  $\frac{1}{2}e^{i\alpha}$ ,  $\frac{1}{2}e^{i\beta}$ , and  $-\frac{1}{2}e^{i\beta}$ , respectively. Therefore,  $b_{2p_+}(t)$  corresponds to  $\vec{OB} = \vec{OA} + \vec{AB}$  and  $b_{2p_-}(t)$  corresponds to  $\vec{OC} = \vec{OA} + \vec{AC}$ . In the triangle, since  $|OA| = |AB| = |AC|$ ,  $\vec{OB}$  is always perpendicular to  $\vec{OC}$  according to Thales's theorem. That is,  $\Delta\Phi(t) = \arg(b_{2p_+}) - \arg(b_{2p_-}) = \pm\pi/2$ . The exact value of  $\Delta\Phi(t)$  can be calculated by substituting the results from the diagonalization as discussed in Appendix A into Eq. (B2). The obtained  $\Delta\Phi(t)$  is shown in Fig. 8(b) and is consistent with the EPD evolution in Fig. 1: the EPD is distributed along the  $45^\circ$  direction when  $-\Delta\Phi(t)/2 = \pi/4$  while the EPD is distributed along the  $-45^\circ$  direction when  $-\Delta\Phi(t)/2 = -\pi/4$ .

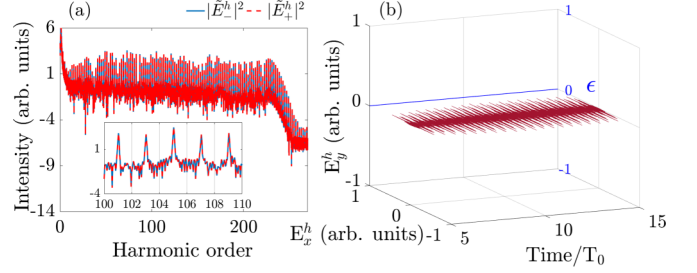


FIG. 9. (a) The high harmonic spectra from the  $1s$  orbital. The inset shows the harmonic spectra in the range of [100, 110] orders. The dashed red and solid blue curves represent the harmonic spectra for the right and left rotating components, respectively. (b) The electric field of the high harmonic radiation in the temporal domain. The ellipticity  $\epsilon$  of the radiation is also presented by the blue line on the time- $\epsilon$  plane.

### APPENDIX C: COMPARISON WITH THE RESULTS FROM THE $1s$ STATE

To demonstrate how large the predicted effect is, we make a comparison between the results from the  $1s$  state and the  $2p_+$  state. The HHG spectra from the  $1s$  state are shown in Fig. 9(a), where the same laser pulse as in Fig. 1 is used. Comparing to the results from the  $2p_+$  state shown in Fig. 3, a similar feature in the frequency domain is found: spectra for the left and right rotating components from the  $1s$  state are nearly the same. Moreover, the time-dependent electric field of the high harmonic emission from the  $1s$  state is shown in Fig. 9(b). One can see that the emission in the temporal domain is always linearly polarized along the  $x$  axis, which is far different from the results from the  $2p_+$  state as shown in Fig. 5. This is because the  $1s$  state has zero angular momentum and the angular momentum of the time-dependent wave function is always 0 during the evolution in response to the linearly polarized laser field. The comparison between the results from the  $1s$  and  $2p_+$  states further indicates that the angular momentum of the target orbital plays a significant role in the polarization state of the harmonic emission.

### APPENDIX D: THE 3D CALCULATIONS

Most results in this work are based on the 2D calculation. Here we also carried out a 3D calculation. The atom is modeled

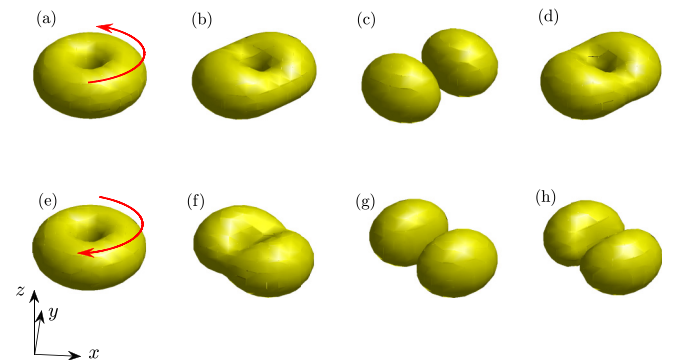


FIG. 10. The snapshots of the EPD of the time-dependent wave function in the 3D calculation at  $t = 0, 2.1T_0, 5.1T_0, 7.9T_0, 9T_0, 10.04T_0, 12.7T_0$ , and  $16T_0$ , respectively

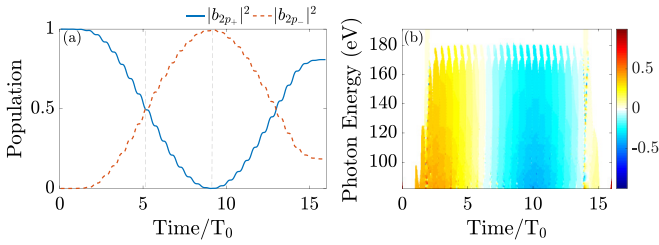


FIG. 11. (a) The populations on the  $2p_{\pm}$  states in the 3D calculation. (b) Ellipticity distribution of the harmonic radiation versus photon energy and time from the 3D calculation.

by a 3D potential  $V(\vec{r}) = -[1 + 9 \exp(-\vec{r}^2)]/\sqrt{\vec{r}^2 + \alpha}$ , in which the soft-core parameter  $\alpha = 1.08$  is used to obtain the correct ionization energy of the valence  $2p$  orbital of Ne. The intensity of the driving laser is the same as that in Fig. 1. The laser wavelength is 1300 nm and the full-width of the laser pulse is  $16T_0$  ( $2T_0$  rising and falling edges and  $12T_0$  plateau) to reduce the computation time. Figure 10 shows the snapshots of the EPD at  $t = 0, 2.1T_0, 5.1T_0, 7.9T_0, 9T_0, 10.04T_0, 12.7T_0$ , and  $16T_0$ , respectively. It is shown that the EPD changes prominently and the 3D time-dependent wave function  $\Psi(\vec{r}, t)$  varies periodically between the current-carrying orbitals with opposite angular momentum  $L_z$  (approximately between the  $2p_{\pm}$  orbitals). Then we calculate the populations on the  $2p_{\pm}$  orbitals as in Fig. 2. The result is shown in Fig. 11(a). One can also see that the populations  $|b_{2p_{\pm}}|^2$  oscillate periodically resembling cosine-like functions with opposite phases. These results indicate that the same evolution of the time-dependent wave function in a linearly polarized laser field occurs in the

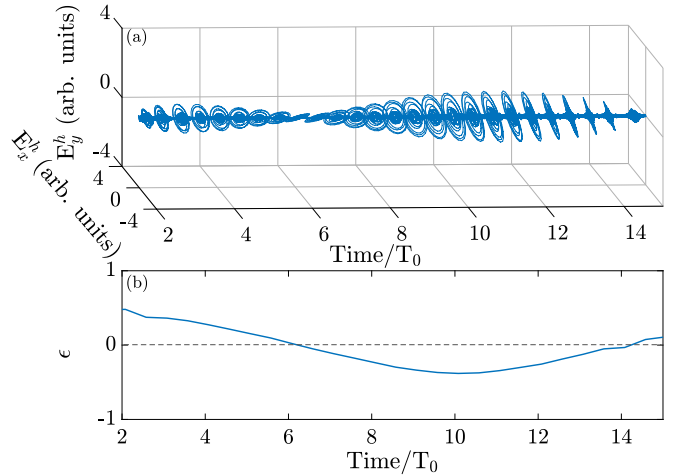


FIG. 12. (a) The electric field of the high harmonic radiation in the temporal domain from the 3D calculation. (b) The corresponding time-dependent ellipticity  $\epsilon$  of the radiation.

3D case. Figure 11(b) shows the ellipticity distribution of the generated high harmonic emission. One can see that the ellipticity oscillates periodically between positive and negative values over time. By synthesizing the high harmonics in the spectrum range of [76 eV, 105 eV], the electric field of the radiation in the temporal domain is obtained. The 3D plot of the obtained electric field is presented in Fig. 12(a). Besides, the corresponding ellipticity versus time is also shown in Fig. 12(b). One can see that the same high harmonic radiation with the ultrafast subpetahertz helicity modulation is obtained.

- [1] J. Miao, P. Charalambous, J. Kirz, and D. Sayre, *Nature (London)* **400**, 342 (1999).
- [2] H. N. Chapman *et al.*, *Nature (London)* **470**, 73 (2011).
- [3] D. M. Villeneuve, P. Hockett, M. J. J. Vrakking, and H. Niikura, *Science* **356**, 1150 (2017).
- [4] S. M. Vinko, O. Ciricosta, B. I. Cho, K. Engelhorn, H.-K. Chung, C. R. D. Brown, T. Burian, J. Chalupský, R. W. Falcone, C. Graves, V. Hájková, A. Higginbotham, L. Juha, J. Krzywinski, H. J. Lee, M. Messerschmidt, C. D. Murphy, Y. Ping, A. Scherz, W. Schlotter, S. Toleikis, J. J. Turner, L. Vysin, T. Wang, B. Wu, U. Zastrau, D. Zhu, R. W. Lee, P. A. Heimann, B. Nagler, and J. S. Wark, *Nature (London)* **482**, 59 (2012).
- [5] W. Zhang *et al.*, *Nature (London)* **509**, 345 (2014).
- [6] M. Schultze, K. Ramasesha, C. D. Pemmaraju, S. A. Sato, D. Whitmore, A. Gandman, J. S. Prell, L. J. Borja, D. Prendergast, K. Yabana, D. M. Neumark, and S. R. Leone, *Science* **346**, 1348 (2014).
- [7] R. W. Schoenlein, S. Chattopadhyay, H. H. W. Chong, T. E. Glover, P. A. Heimann, C. V. Shank, A. A. Zholents, and M. S. Zolotarev, *Science* **287**, 2237 (2000).
- [8] N. Čutić, F. Lindau, S. Thorin, S. Werin, J. Bahrtdt, W. Eberhardt, K. Hollmack, C. Erny, A. L'Huillier, and E. Mansten, *Phys. Rev. ST Accel. Beams* **14**, 030706 (2011).
- [9] E. Allaria *et al.*, *Nat. Photon.* **6**, 699 (2012).
- [10] V. López-Flores, J. Arabski, C. Stamm, V. Halté, N. Pontius, E. Beaurepaire, and C. Boeglin, *Phys. Rev. B* **86**, 014424 (2012).
- [11] P. M. Paul, E. S. Toma, P. Breger, G. Mullot, F. Augé, Ph. Balcou, H. G. Muller, and P. Agostini, *Science* **292**, 1689 (2001).
- [12] G. Sansone, E. Benedetti, F. Calegari, C. Vozzi, L. Avaldi, R. Flammini, L. Poletto, P. Villoresi, C. Altucci, R. Velotta, S. Stagira, S. De Silvestri, and M. Nisoli, *Science* **314**, 443 (2006).
- [13] J. Seres, V. S. Yakovlev, E. Seres, Ch. Strelti, P. Wobrauschek, Ch. Spielmann, and F. Krausz, *Nat. Phys.* **3**, 878 (2007).
- [14] E. Goulielmakis, M. Schultze, M. Hofstetter *et al.*, *Science* **320**, 1614 (2008).
- [15] W. Boutu, S. Haessler, H. Merdji, P. Breger, G. Waters, M. Stankiewicz, L. J. Frasinski, R. Taieb, J. Caillat, A. Maquet, P. Monchicourt, B. Carre, and P. Salieres, *Nat. Phys.* **4**, 545 (2008).
- [16] M. A. Fareed, M. A. Fareed, V. V. Strelkov, N. Thiré, S. Mondal, B. E. Schmidt, F. Légaré, and T. Ozaki, *Nat. Commun.* **8**, 16061 (2017).
- [17] J. Li, X. Ren, Y. Yin, K. Zhao, A. Chew, Y. Cheng, E. Cunningham, Y. Wang, S. Hu, Y. Wu, M. Chini, and Z. Chang, *Nat. Commun.* **8**, 186 (2017).
- [18] T. Gaumnitz, A. Jain, Y. Pertot, M. Huppert, I. Jordan, F. Ardana-Lamas, and H. J. Wörner, *Opt. Express* **25**, 27506 (2017).
- [19] D. M. Reich and L. B. Madsen, *Phys. Rev. Lett.* **117**, 133902 (2016).

- [20] O. Smirnova, Y. Mairesse, S. Patchkovskii, N. Dudovich, D. Villeneuve, P. Corkum, and M. Y. Ivanov, *Nature (London)* **460**, 972 (2009).
- [21] D. Shafir, H. Soifer, B. D. Bruner, M. Dagan, Y. Mairesse, S. Patchkovskii, M. Yu. Ivanov, O. Smirnova, and N. Dudovich, *Nature (London)* **485**, 343 (2012).
- [22] J. Wu, M. Meckel, L. Ph. H. Schmidt, M. Kunitski, S. Voss, H. Sann, H. Kim, T. Jahnke, A. Czasch, and R. Dörner, *Nat. Commun.* **3**, 1113 (2012).
- [23] P. M. Kraus, B. Mignolet, D. Baykusheva, A. Rupenyany, L. Horný, E. F. Penka, G. Grassi, O. I. Tolstikhin, J. Schneider, F. Jensen, L. B. Madsen, A. D. Bandrauk, F. Remacle, and H. J. Wörner, *Science* **350**, 790 (2015).
- [24] L. He, Q. Zhang, P. Lan, W. Cao, X. Zhu, C. Zhai, F. Wang, W. Shi, M. Li, X. Bian, P. Lu, and A. D. Bandrauk, *Nat. Commun.* **9**, 1108 (2018); P. Lan, M. Ruhmann, L. He, C. Zhai, F. Wang, X. Zhu, Q. Zhang, Y. Zhou, M. Li, M. Lein, and P. Lu, *Phys. Rev. Lett.* **119**, 033201 (2017).
- [25] X. Liu, P. Li, X. Zhu, P. Lan, Q. Zhang, and P. Lu, *Phys. Rev. A* **95**, 033421 (2017).
- [26] P. B. Corkum, *Phys. Rev. Lett.* **71**, 1994 (1993).
- [27] I. Powis, *Adv. Chem. Phys.* **138**, 267 (2008).
- [28] C. Lux, M. Wollenhaupt, T. Bolze, Q. Liang, J. Kohler, C. Sarpe, and T. Baumert, *Angew. Chem. Int. Ed.* **51**, 5001 (2012).
- [29] Y. Song, C. Zhang, W. Liu, X. Li, H. Long, K. Wang, B. Wang, and P. Lu, *Opt. Express* **26**, 18448 (2018); F. Wang, S. Ke, C. Qin, B. Wang, H. Long, K. Wang, and P. Lu, *Opt. Laser Technol.* **103**, 272 (2018); X. Ma, Y. Zhou, N. Li, M. Li, and P. Lu, *ibid.* **108**, 235 (2018).
- [30] I. Radu, K. Vahaplar, C. Stamm, T. Kachel, N. Pontius, H. A. Dürr, T. A. Ostler, J. Barker, R. F. L. Evans, R. W. Chantrell, A. Tsukamoto, A. Itoh, A. Kirilyuk, Th. Rasing, and A. V. Kime, *Nature (London)* **472**, 205 (2011).
- [31] G. Lambert, B. Vodungbo, J. Gautier, B. Mahieu, V. Malka, S. Sebban, P. Zeitoun, J. Luning, J. Perron, A. Andreev, S. Stremoukhov, F. Ardana-Lamas, A. Dax, C. P. Hauri, A. Sardinha, and M. Fajardo, *Nat. Commun.* **6**, 6167 (2015).
- [32] O. Kfir, P. Grychto, E. Turgut, R. Knut, D. Zusin, D. Popmintchev, T. Popmintchev, H. Nembach, J. M. Shaw, A. Fleischer, H. Kapteyn, M. Murnane, and O. Cohen, *Nat. Photon.* **9**, 99 (2015).
- [33] T. Fan *et al.*, *Proc. Natl. Acad. Sci. USA* **112**, 14206 (2015).
- [34] A. Ferré, C. Handschin, M. Dumergue, F. Burgy, A. Comby, D. Descamps, B. Fabre, G. A. Garcia, R. Géneaux, L. Merceron, E. Mével, L. Nahon, S. Petit, B. Pons, D. Staedter, S. Weber, T. Ruchon, V. Blanchet, and Y. Mairesse, *Nat. Photon.* **9**, 93 (2014).
- [35] D. B. Milošević, W. Becker, and R. Kopold, *Phys. Rev. A* **61**, 063403 (2000); D. B. Milošević, *Opt. Lett.* **40**, 2381 (2015).
- [36] K. J. Yuan and A. D. Bandrauk, *Phys. Rev. Lett.* **110**, 023003 (2013).
- [37] A. Fleischer, O. Kfir, T. Diskin, P. Sidorenko, and O. Cohen, *Nat. Photon.* **8**, 543 (2014).
- [38] K. M. Dorney, J. L. Ellis, C. Hernández-García, D. D. Hickstein, C. A. Mancuso, N. Brooks, T. Fan, G. Fan, D. Zusin, C. Gentry, P. Grychto, H. C. Kapteyn, and M. M. Murnane, *Phys. Rev. Lett.* **119**, 063201 (2017).
- [39] X. Xie, A. Scrinzi, M. Wickenhauser, A. Baltuška, I. Barth, and M. Kitzler, *Phys. Rev. Lett.* **101**, 033901 (2008).
- [40] X. Zhou, R. Lock, N. Wagner, W. Li, H. C. Kapteyn, and M. M. Murnane, *Phys. Rev. Lett.* **102**, 073902 (2009).
- [41] L. Medišauskas, J. Wragg, H. van der Hart, and M. Yu. Ivanov, *Phys. Rev. Lett.* **115**, 153001 (2015).
- [42] D. D. Hickstein, F. J. Dollar, P. Grychto, J. L. Ellis, R. Knut, C. Hernández-García, D. Zusin, C. Gentry, J. M. Shaw, T. Fan, K. M. Dorney, A. Becker, A. Jaroń-Becker, H. C. Kapteyn, M. M. Murnane, and C. G. Durfee, *Nat. Photon.* **9**, 743 (2015).
- [43] H. Xie, M. Li, S. Luo, Y. Li, J. Tan, Y. Zhou, W. Cao, and P. Lu, *Opt. Lett.* **43**, 3220 (2018).
- [44] X. Zhu, Q. Zhang, W. Hong, P. Lu, and Z. Xu, *Opt. Express* **19**, 24198 (2011).
- [45] I. Barth and M. Lein, *J. Phys. B* **47**, 204016 (2014).
- [46] I. Barth and J. Manz, *Phys. Rev. A* **75**, 012510 (2007).
- [47] I. Barth, J. Manz, Y. Shigeta, and K. Yagi, *J. Am. Chem. Soc.* **128**, 7043 (2006).
- [48] I. Barth and J. Manz, *Angew. Chem. Int. Ed.* **45**, 2962 (2006).
- [49] J. Tan, Y. Zhou, M. Li, M. He, Y. Liu, and P. Lu, *Opt. Express* **26**, 20063 (2018); J. Tan, Y. Li, Y. Zhou, M. He, Y. Chen, M. Li, and P. Lu, *Opt. Quantum Electron* **50**, 57 (2018).
- [50] M. D. Feit, J. A. Fleck Jr., and A. Steiger, *J. Comput. Phys.* **47**, 412 (1982).
- [51] T. Herath, L. Yan, S. K. Lee, and W. Li, *Phys. Rev. Lett.* **109**, 043004 (2012).
- [52] S. Eckart, M. Kunitski, M. Richter, A. Hartung, J. Rist, F. Trinter, K. Fehre, N. Schlott, K. Henrichs, L. P. H. Schmidt, T. Jahnke, M. Schöffler, K. Liu, I. Barth, J. Kaushal, F. Morales, M. Ivanov, O. Smirnova, and R. Dörner, *Nat. Phys.* **14**, 701 (2018).
- [53] J. Sakurai and J. Napolitano, in *Modern Quantum Mechanics*, 2nd ed. (Addison-Wesley, Reading, MA, 2011), p. 346.
- [54] N. V. Vitanov, A. A. Rangelov, B. W. Shore, and K. Bergmann, *Rev. Mod. Phys.* **89**, 015006 (2017).
- [55] D. Baykusheva, Md S. Ahsan, N. Lin, and H. J. Wörner, *Phys. Rev. Lett.* **116**, 123001 (2016).
- [56] C. C. Chirilă, I. Dreissigacker, E. V. van der Zwan, and M. Lein, *Phys. Rev. A* **81**, 033412 (2010).
- [57] M. Wollenhaupt, A. Präkelt, C. Sarpe-Tudoran, D. Liese, and T. Baumert, *J. Opt. B* **7**, S270 (2005).
- [58] M. Wollenhaupt, A. Präkelt, C. Sarpe-Tudoran, D. Liese, T. Bayer, and T. Baumert, *Phys. Rev. A* **73**, 063409 (2006).
- [59] M. Wollenhaupt, D. Liese, A. Präkelt, C. Sarpe-Tudoran, and T. Baumert, *Chem. Phys. Lett.* **419**, 184 (2006).
- [60] C. Chen, Z. Tao, C. Hernández-García, P. Matyba, A. Carr, R. Knut, O. Kfir, D. Zusin, C. Gentry, P. Grychto, O. Cohen, L. Plaja, A. Becker, A. Jaron-Becker, H. Kapteyn, and M. Murnane, *Sci. Adv.* **2**, e1501333 (2016).
- [61] C. Jin, A.-T. Le, and C. D. Lin, *Phys. Rev. A* **83**, 023411 (2011).
- [62] B. Vodungbo, J. Gautier, G. Lambert, A. B. Sardinha, M. Lozano, S. Sebban, M. Ducouso, W. Boutu, K. Li, B. Tudu, M. Tortarolo, R. Hawaldar, R. Delaunay, V. López-Flores, J. Arabski, C. Boeglin, H. Merdji, P. Zeitoun, and J. Luning, *Nat. Commun.* **3**, 999 (2012).
- [63] C. D. Stanciu, F. Hansteen, A. V. Kimel, A. Kirilyuk, A. Tsukamoto, A. Itoh, and Th. Rasing, *Phys. Rev. Lett.* **99**, 047601 (2007).
- [64] S. Mathias, C. La-O-Vorakiat, P. Grychto, P. Granitzka, E. Turgut, J. M. Shaw, R. Adam, H. T. Nembach, M. E. Siemens, S. Eich, C. M. Schneider, T. J. Silva, M. Aeschlimann, M. M. Murnane, H. C. Kapteyn *et al.*, *Proc. Natl. Acad. Sci. USA* **109**, 4792 (2012).